Engineering Structures 126 (2016) 417–431

Contents lists available at ScienceDirect

Engineering Structures

journal homepage: www.elsevier.com/locate/engstruct

Performance evaluation of full-scale tuned liquid dampers (TLDs) for vibration control of large wind turbines using real-time hybrid testing

Zili Zhang [a,b], Andrea Staino [c], Biswajit Basu [c,*], Søren R.K. Nielsen [a]

[a] Department of Civil Engineering, Aalborg University, 9000 Aalborg, Denmark
[b] Department of Engineering, Aarhus University, 8000 Aarhus C, Denmark
[c] Department of Civil, Structural & Environmental Engineering, School of Engineering, Trinity College Dublin, Dublin 2, Ireland

ARTICLE INFO

Article history:
Received 30 October 2015
Revised 4 July 2016
Accepted 6 July 2016
Available online 10 August 2016

Keywords:
Tuned liquid dampers
Wind turbines
Lateral tower vibration
Real-time hybrid testing
Full scale test

ABSTRACT

Tuned liquid dampers (TLDs) utilize the sloshing motion of the fluid to suppress structural vibrations and become a natural candidate for vibration control of large flexible wind turbines. Special structures such as wind turbine towers have characteristics and exhibit behavior which are significantly different from conventional civil engineering structures. In addition, the stochastic aerodynamic load generated from the turbulence is different from what is generated on conventional tall structures, due to rotationally sampled spectra. Experimental studies on the evaluation of full scale TLDs to control vibration of such special facilities like wind turbine towers are absent in literature. In this paper, the performance of a full-scale TLD in mitigating lateral tower vibrations of multi-megawatt wind turbines is evaluated through the real-time hybrid testing (RTHT). Lateral tower vibrations of wind turbines are normally lightly damped due to low or even negative aerodynamic damping, and large amplitude vibrations induced by wind and ocean wave loads in the lateral direction may significantly shorten the fatigue life of the tower. In the RTHT, the full-scale TLD is tested as the physical substructure while the wind turbine is modeled using a 13-degree-of-freedom (13-DOF) aeroelastic model. Wind turbines with 2 MW and 3 MW capacities have been considered and cases of the TLD with and without damping screens have been tested. Further, the effect of tuning ratios on the damper performance has been studied by changing the mean water level of the tank. Finally, comparison has been performed between the experimental results and the results from an theoretical model of the TLD-wind turbine system. The present study provides strong support and useful guidelines for the application of TLDs in large wind turbines.

1. Introduction

Recent development in the wind energy industry aims at obtaining more economic and productive configurations in order to compete in the energy sector. Multi-megawatt wind turbines are designed with increasingly larger rotors and higher towers, in order to capture more energy throughout their lifetime and, thereby, reduce the cost of energy. As wind turbines grow in size, the stiffness of the blades and the tower are not increased proportionally, rendering the structure more sensitive to dynamic excitations. The large amplitude vibrations may significantly shorten the fatigue life of the structural components and reduce the operational efficiency in converting the wind energy to electrical power.

Normally, flap-wise blade vibration and fore-aft tower vibration (along-wind direction) are highly damped due to the strong aerodynamic damping as long as the flow is attached at the blade [1]. In contrast, edgewise blade vibration and lateral tower vibration (side-side direction) are related with insignificant aerodynamic damping [1,2]. Hence, these modes of vibrations may be prone to large amplitude vibrations. There is also a possibility of aeroelastic instability in the lateral tower mode for some combinations of aerodynamic properties and operational conditions, especially for the parked turbine with nacelle yaw errors [3]. Moreover, for offshore wind turbines placed at shallow water, the wave load may act in a different direction of the mean wind direction due to refraction, and significant lateral tower vibrations may be initiated by the wave load in combination with the resultant aerodynamic loads from the three blades in the lateral direction. Finally, due to the coupling between the lateral tower vibration with the drivetrain torsional motion, the unfavorable tower vibrations will

* Corresponding author.
E-mail addresses: zili_zhang@eng.au.dk (Z. Zhang), stainoa@tcd.ie (A. Staino), basub@tcd.ie (B. Basu), srkn@civil.aau.dk (S.R.K. Nielsen).

http://dx.doi.org/10.1016/j.engstruct.2016.07.008
0141-0296/

increase the fluctuations of the generator torque, and hence the quality of the generated power. Therefore, excessive lateral tower vibrations not only lead to significantly reduced fatigue life of the support structure, but also influence the quality of generated power from the turbine.

Structural control technologies, which have achieved significant success in mitigating vibrations of civil engineering structures, are drawing more and more attention from both wind energy industry and academia [4,5]. Several passive and active control devices have been developed and implemented for tower vibration control. In industry, pendulum dampers immersing in oil have been proposed [6] to be mounted inside the wind turbine tower, and highly reduced 2-degree-of-freedom (2-DOF) models have been established for this system. In academia, theoretical investigations have been performed on the effectiveness of a tuned mass damper (TMD) [7] and tuned liquid column damper (TLCD) [8] for mitigating along-wind tower vibrations, ignoring the aerodynamic properties of the blades. To yield more realistic results, an advanced modeling tool has been developed and incorporated into the aeroelastic code, FAST (Fatigue, Aerodynamics, Structures and Turbulence), allowing the investigation of passive TMDs in vibration control of offshore wind turbine systems [9]. A series of shaking table tests have been carried out to evaluate the performance of the ball vibration absorber (BVA) on vibration control of a reduced scale wind turbine model, through which the effectiveness of the passive damping device was proven [10]. However, the focus of this study is still on the fore-aft tower vibration without considering the aerodynamic damping. Therefore, it is of great importance and necessity to carry out a comprehensive investigation on structural control of the lightly-damped lateral tower vibrations.

Tuned liquid damper (TLD), which consists of a tank partially filled with liquid, is a passive control device for suppressing structural vibrations. The fundamental sloshing frequency of the liquid is normally tuned to the fundamental frequency of the primary structure. When the TLD is excited by the motion of the primary structure, the liquid inside the tank begins to slosh, imparting inertial forces onto the structure, out of phase with its motion, thus absorbing and dissipating energy. The main advantages of the TLD are the ease of fabrication and installation, especially where space constraints exist, and minimal maintenance after installation, which make the device cost-effective. The TLD has been proved to effectively control the wind-induced vibration of structures [11,12]. It is also proposed for seismic control of structures. Both experimental and theoretical studies [13–15] have shown that TLDs successfully suppress vibrations of the flexible structures subjected to earthquake excitations.

The main difficulties associated with TLDs arise from the nonlinear nature of the sloshing liquid, which makes modeling and designing of these devices challenging. Different methods have been employed to predict the response of sloshing liquid. Equivalent mechanical models based on TMD analogy [16,17] simplify the TLD into an equivalent tuned mass damper, with the equivalent mass, stiffness and damping calibrated from the experimental results. This model is able to predict the energy dissipation through liquid sloshing and is useful in the preliminary design of the TLD. However, the nonlinear fluid response cannot be captured. Nonlinear shallow water wave theory [18,19] has been proposed for predicting the response of fluid sloshing in rectangular tanks. Although the nonlinear shallow-water wave equations can be numerically solved, it is computational inefficient and does not provide an effective design tool for engineering application. Modal expansion techniques [20–22] have been used for modeling the sloshing problem, where the fluid flow is assumed to be inviscid, irrotational, incompressible and without rigid-body rotations. The velocity potential and the free surface are expressed as a summation of sloshing modes, and a system of coupled ordinary differential equations are developed by applying calculus of variations [20,21].

In principle, all the above-mentioned models have errors in capturing the real dynamic characteristics of the sloshing liquid and the control force generated by the TLD. It turns out to be necessary to obtain the response of the TLD-structure system through experiments. However, to the best of our knowledge, only reduced-scale tests have been carried out for the evaluating the performance of small TLDs on vibration control of structures [14,18,19]. The scaled down model of the system tested in lab conditions will essentially suffer from the scale effect, particularly with respect to the liquid behavior in the damper (e.g., due to viscous effect), and it may be a challenge to keep appropriate proportion with dynamic similarities for the primary structure and the liquid inside the TLD.

To circumvent these problems, a state-of-the-art testing method, real-time hybrid testing (RTHT) [23–25] turns out to be a feasible solution. The fundamental idea of the RTHT is to split the entire system into two parts: a numerical substructure and a physical substructure. The former will be simulated in the computer by a developed numerical model. The latter, which generally has a complicated dynamic behavior (nonlinear or load rate-dependent), is manufactured and tested using dynamic testing equipment (shaking table or dynamic actuators) [14,26]. This method has several advantages, such as the reduced cost of the experiment, safe evaluation of structures at extreme states, and especially the possibility of manufacturing full scale physical substructure, making the full-scale test of TLDs applicable. The RTHT has been widely adopted for the performance evaluation of energy dissipating and vibration absorbing devices in building structures, such as elastomeric dampers [26], MR dampers [27] and TMDs [28]. It has also been employed to investigate a reduced-scale TLD for the vibration control of earthquake excited buildings, where the structure is modeled by a 3-degree-of-freedom (3-DOF) model [14].

Although widely investigated in building structures, the RTHT of TLDS for vibration control has not been applied to wind turbine structures yet. Quite different from traditional civil engineering structures, a wind turbine is a highly coupled system with extra subsystems such as the pitch controller, the yaw controller and the generator. Vibrations of the rotating blade, the tower and the drivetrain are coupled with each other, and are influenced by the above-mentioned subsystems as well. These generate loads such as harmonic loading from wind shear and gravity, and effects such as centrifugal stiffening. Therefore, wind turbines need to be modeled as a complete aeroelastic system, rather than the highly reduced order models for building structures. Further, due to the rotational effect of the rotor, rotational sampled turbulence [30] should be applied to the blades rather than the conventional turbulence field that is applied to tall buildings or bridges. Due to longitudinal correlation of the incoming turbulent wind, a certain periodicity is present as spectral peaks at 1 Ω, 2 Ω, 3 Ω. . .in the frequency domain representation of the rotational sampled turbulence, where Ω is the rotational speed of the rotor.

In the study reported here, the performance of the TLD in suppressing lateral tower vibrations of multi-megawatt wind turbines is evaluated through RTHT. A full scale TLD is manufactured and tested as the physical substructure, while a highly-coupled 13-DOF aeroelastic wind turbine model is employed as the numerical substructure. The dynamic responses of the wind turbine system are numerically calculated in real time using the 13-DOF model formulated in Matlab/Simulink. The excitations exerted to the model are the measured control force from the TLD, and the pre-calculated modal loads induced by rotational sampled turbulence (with due consideration of the aerodynamic damping). Both the 3 MW and 2 MW wind turbines have been considered in establishing the Simulink model. Cases of the TLD with and without

damping screens have been tested for evaluating the control effect of the damper with different energy dissipations of the sloshing. Further, various values of the tuning ratio, the mean wind speed and the turbulence intensity are considered in the RTHT, so that a systematic evaluation of the damper performance can be revealed. Finally, simulation results from a pure theoretical model are compared with the recorded results from the RTHT, and the acceptable agreement verifies the accuracy of both the RTHT and the theoretical model. The investigated full-scale TLD can be directly applied to real wind turbine structures without any scaling problem.

2. Real-time hybrid testing

2.1. General description

The RTHT presented in this paper has been carried out using the MTS real-time hybrid testing system at Trinity College Dublin, Ireland [29]. The system allows to simultaneously combine physical testing of the TLD with the computer model of the wind turbine system. The RTHT system is mainly composed of the following:

(1) a host PC running Matlab/Simulink, which is used to program Simulink models of the wind turbine system using the Real-Time Windows Target toolbox;
(2) a target PC with the shared common random access memory network (SCRAMNet), on which compiled Simulink models are downloaded and the real-time simulation is run in Mathworks xPC Target environment;
(3) a hybrid controller host PC, which runs the graphical user interface to the MTS servo-controller. The software Structural Test System (STS) can be used to calibrate and tune instrumentation, servo-valves and actuators prior to a test;
(4) a MTS servo-controller hardware with SCRAMNet, which includes a digital PID actuator controller, signal conditioners, data acquisition system and interlock mechanisms. The controller is preset to run at a frequency of 1024 Hz, which is the update rate for the servo-valve commands;
(5) a hydraulic actuator equipped with displacement and force sensors, which physically operates the desired commend to the physical substructure and allows to measure the quantities of interest.

The communication through the target PC and the MTS controller is managed through the SCRAMNet, which is a local high-speed network ring. Such local high-speed connections drastically reduce delays and make it possible to perform continuous and/or real-time hybrid simulation. Using SCRAMNet, memory-writes to the replicated shared memory at one computer are instantly sent to all other replicated shared memories at 150 MB/s via high-speed fiber optic cables.

A schematic diagram representing the RTHT system is illustrated in Fig. 1. The MTS controller accepts a displacement or force command and generates the proper command signal for the servo-valve that moves the actuator to the commanded position. In order to access the MTS controller from the target PC, Simulink blocks are available to perform input/output operations through the SCRAMNet memory associated with the controller. The blocks contain the I/O signals that allow interaction with the experimental specimen. Hence, force and displacement commands can be sent from the target PC to the actuator, while measurement from the transducers can be fed back to the real-time simulation environment.

2.2. Implementation of the hybrid model

Fig. 2 depicts the conceptual illustrations of the RTHT for the TLD-wind turbine system carried out in this paper. At each time step, the discrete equations of motion of the 13-DOF wind turbine model are solved on the target PC. The numerically obtained lateral tower vibration is sent as a displacement command over the SCRAMNet. The MTS controller generates an appropriate signal for the servo-valve which attempts to move the actuator to the commanded position. The actual displacement of the actuator and the interacting force (control force/sloshing force) measured from the load cell are fed back to the SCRAMNet and accessed by the target PC. With this TLD-generated control force, the equations of motion of the wind turbine system, where a TLD is installed, are solved numerically, and the displacement command is sent to the controller again. This process is carried out in real-time.

Applying the load history at fast rates, rather than a ramp-hold load history to the actuator, improves the performance and accuracy of the experiment by eliminating the hold phase and associated force relaxation [30]. Better control of the actuator is also achieved through a fast-rated command signal. Further, high performance actuators coupled with fast hybrid test methods can capture the rate-dependent behavior of the physical substructure, such as the TLD. In most of the recent hybrid tests [29–31], the MTS controller runs at a sampling rate of 1024 Hz (1/1024 s sampling time) to control the motion of the servo-hydraulic actuator using the SCRAMNet. When the integration time step of the numerical substructure is larger than 1/1024 s (for nonlinear finite element models), the predictor-corrector technique [24,31] has been widely employed to generate the displacement command at the required rate (1024 Hz) and to synchronize the hybrid simulation.

In the present hybrid system, the integration time step of the numerical substructure (the 13-DOF wind turbine model) is set to be equal to the sampling time of the MTS controller (1/1024 s), since no iterations are needed for solving the numerical model and the actual task execution time is less than 1/1024 s. Therefore, synchronization is achieved without using the predictor-corrector technique.

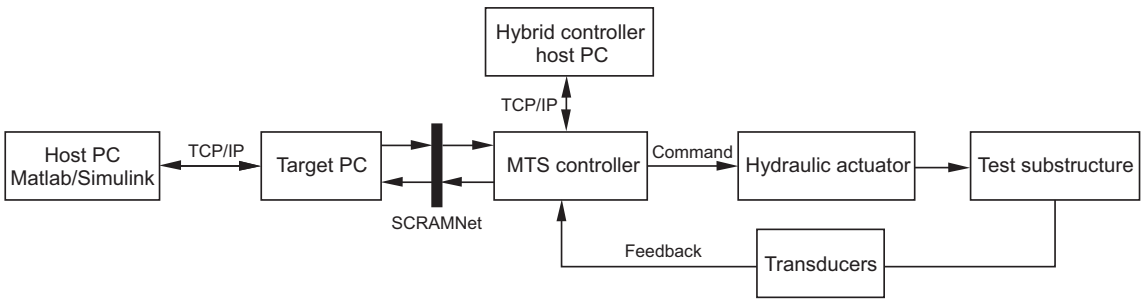

Fig. 1. Layout of the RTHT system.

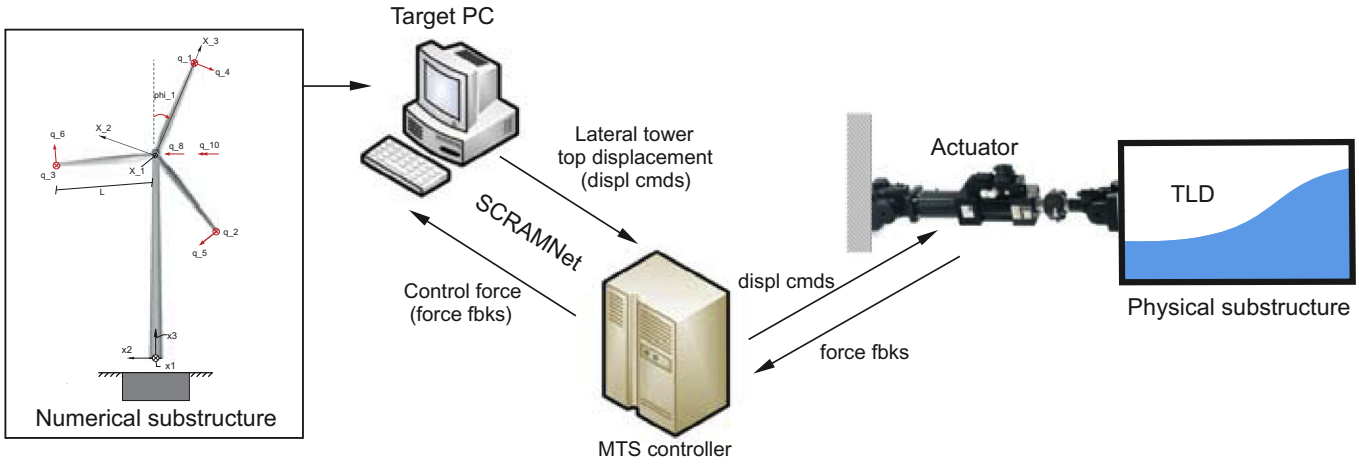

Fig. 2. Conceptual view of the RTHT for the TLD-wind turbine system.

There is an inherent lag in the displacement response of servo-hydraulic actuator versus the command displacement. Consequently, the measured restoring forces are delayed relative to the command signal. To compensate for this delay, the compensation technique proposed in [25] has been applied here. The time lag of the actuator response is measured first and polynomial extrapolation procedure is then used to predict the command of the actuator by advancing the current time in the algorithm by the delay time. Detailed results of the delay compensation will be given later.

2.3. Numerical substructure: the 13-DOF wind turbine model

The numerical substructure of the up-wind wind turbine system shown in Fig. 3 is a 13-DOF aeroelastic model. The motions of the tower and the drivetrain are described in a fixed, global (X_1, X_2, X_3)-coordinate, while the motion of each blade is described in a moving, local (x_1, x_2, x_3)-coordinate system with its origin at the center of the hub. Assuming a constant rotational speed Ω of the rotor, the position of the local coordinate system attached to blade j is specified by the azimuthal angle $\Psi_j(t)$:

$$\Psi_j(t) = \Omega t + \frac{2\pi}{3}(j-1),\ j = 1,2,3 \tag{1}$$

which is positive when rotating clockwise as observed from an upwind position.

Each blade is modeled as a Bernoulli-Euler beam with variable mass per unit length and variable bending stiffness. The flap-wise and edgewise motions of the three blades are modeled by the DOFs $q_j(t)$ and $q_{j+3}(t)$, $j = 1,2,3$, indicating the tip displacement in the positive x_1-direction and the negative x_2-direction, respectively. The related mode shapes are taken as the undamped fundamental eigenmodes $\Phi_f(x_3)$ and $\Phi_e(x_3)$ in the flap-wise and edgewise directions with $\Omega = 0$.

The tower motion is defined by the translational DOFs $q_7(t)$ and $q_8(t)$ in the global X_1- and X_2-directions, and the rotational DOFs $q_9(t), q_{10}(t), q_{11}(t)$ in the global X_1-, X_2- and X_3-directions. Hence, the lateral tower vibration is modeled by the top elastic displacement $q_8(t)$ and top elastic rotation $q_9(t)$, using cubic shape functions [32]. At each time step, the calculated $q_8(t)$ is sent to the MTS controller as the displacement command.

The drivetrain shown in Fig. 4 is modeled by the DOFs $q_{12}(t)$ and $q_{13}(t)$, indicating the deviations of the rotational angles at the hub and the generator from the nominal rotational angles Ωt and $N\Omega t$, respectively, where N is the gear ratio. Correspondingly, $\dot{q}_{12}(t)$ and $\dot{q}_{13}(t)$ are the deviations of the rotational speeds at the hub and the generator from the nominal values. J_r and J_g denote the mass moment of inertia of the rotor and the generator, and k_r and k_g denote the St.Venant torsional stiffness of the rotor shaft and the generator shaft.

Assuming linear structural dynamics and substituting the kinetic and potential energies into the Euler-Lagrange equation [33], the equations of motion of the 13-DOF model are obtained of the form:

$$\mathbf{M}(t)\ddot{\mathbf{q}}(t) + \mathbf{C}(t)\dot{\mathbf{q}}(t) + \mathbf{K}(t)\mathbf{q}(t) = \mathbf{f}_e(t) \tag{2}$$

where $\mathbf{q}(t)$ is the DOFs vector. $\mathbf{M}(t)$ is the mass matrix, $\mathbf{C}(t)$ is the damping matrix including the structural and gyroscopic damping, and $\mathbf{K}(t)$ is the stiffness matrix taking into account the geometric and gyroscopic stiffness. All the indicated system matrices contain the azimuthal angle $\Psi_j(t)$ and are thus time-varying. This is because the DOFs of the blades are modeled in the moving coordinate system, while others are formulated in a fixed coordinate system. Detailed expressions of the system matrices can be found in [32]. $\mathbf{f}_e(t)$ is the external load vector work conjugated to $\mathbf{q}(t)$, including the non-linear aerodynamic loads and the generator torque.

In agreement with [34], the turbulence modeling is based on Taylor's hypothesis of frozen turbulence, corresponding to a frozen filed convected into the rotor plane in global X_1-direction with a mean velocity V_0 and a turbulence intensity I. The frozen field is assumed to be homogeneous and isotropic, with a covariance structure given by [35]. Calibrated from this theoretical covariance structure, the 1st order AR model as proposed by [36] performs a 1st order filtering of the white noise input, resulting in continuous, non-differentiable sample curves of the turbulence field at the rotor plane. Next, the turbulence encountered in the moving frame of reference fixed to the rotating blade is obtained by linear interpolation between the turbulence at different grid points in the fixed frame of reference, resulting in the rotational sampled turbulence.

With the generated rotational sampled turbulence, the aerodynamic loads along the blade can be calculated by the widely-used Blade Element Momentum (BEM) method with Prandtl's tip loss factor and Glauert correction [37]. BEM analysis is carried out by combining momentum theory and blade element theory, and allows to have a realistic estimate of the wind loading to which the rotor is subjected to. It is one of the standard methods (probably the most popular one) for aerodynamic load calculation in both wind energy industry and academia. Non-linear aeroelasticity is

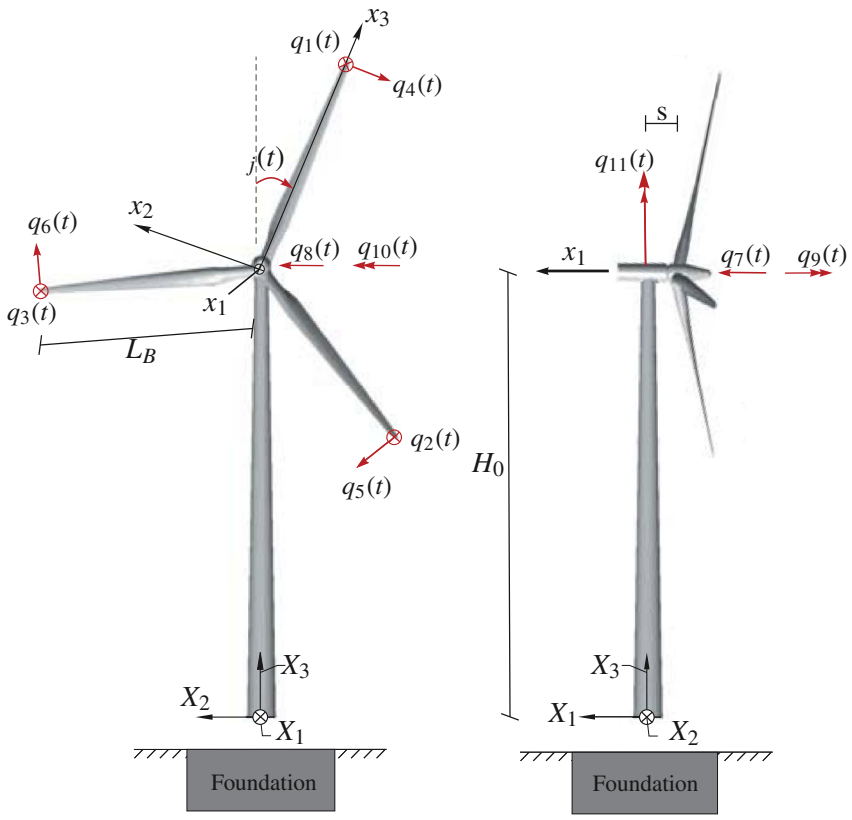

Fig. 3. The 13-DOF aeroelastic wind turbine model. Definition of fixed and moving coordinate systems and the degrees of freedom $q_1(t), \ldots, q_{11}(t)$.

considered by introducing the local deformation velocities of the blade into calculations of the flow angle and the angle of attack. As a result, this model possesses high aerodynamic damping in the blade flap-wise and the fore-aft tower vibrations, but relatively low aerodynamic damping in the blade edgewise and the lateral tower vibrations. The tower shadowing effect has not been considered in the model, since it's much more significant for the down-wind wind turbine than for the up-wind one considered here.

Further, a full-span rotor-collective pitch controller is included in the model with time delay modeled by a first order filter. The pitch demand is modeled by a PI controller with feedback from $q_{12}(t)$ and $\dot{q}_{12}(t)$.

The 13-DOF model is formulated in Matlab/Simulink, where all the terms are discretized and the backward Euler method has been used for solving the discrete equations of motion. The time-varying system matrices are handled by user-defined Matlab functions. Two blocks, one receives inputs from SCRAMNet to the 13-DOF model and one sends commands from the 13-DOF model to SCRAMNet, are included in the Simulink model as well.

2.4. Experimental substructure test setup

Fig. 5 shows a photograph of the test setup and the physical substructure (the TLD). The setup has a hydraulic actuator in the horizontal direction, a reaction frame and the data acquisition system. The MTS 244 actuator, with a load capacity of 150 kN and a maximum stroke of ±125 mm, is bolted to the left side of the TLD. One load cell and one linear variable displacement transducer (LVDT) are attached at the actuator to measure the interaction force and the actuator displacement. The full-size TLD is made up of a closed rectangular tank, with a inner size of 1.93 m (length) × 0.59 m (width) × 1.2 m (height). Since the width of the tank is much smaller than the length, it is expected the sloshing of the water is predominately 2-dimensional. The TLD is suspended to top of the reaction frame by four steel cables in order to minimize the friction when the tank is enforced to move by the actuator. Further, a capacitance wave gauge (with a sampling rate of 10 Hz) is installed at the left end-wall of the tank to measure the liquid surface elevation.

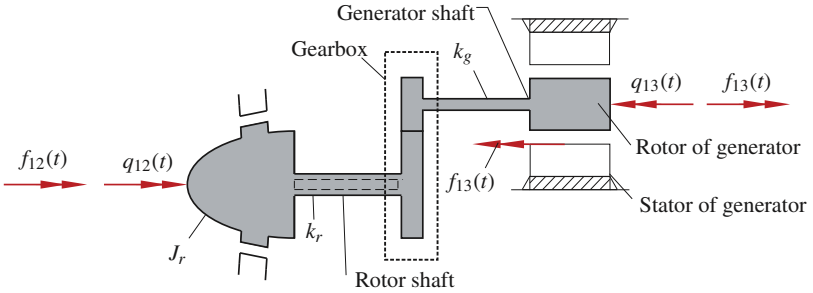

Fig. 4. 2-DOF model of the flexible drivetrain with odd number of gear stages. Definition of degrees of freedom $q_{12}(t)$ and $q_{13}(t)$.

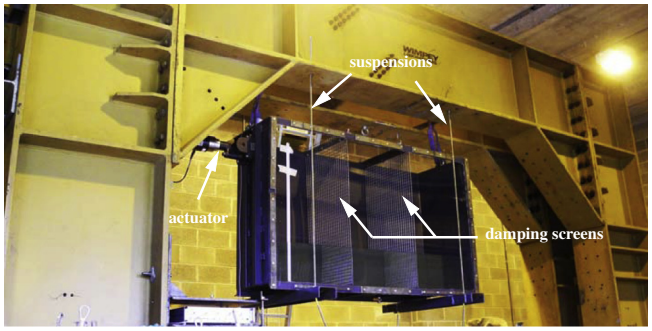

Fig. 5. Test setup and the physical substructure (the TLD).

The tank with installed damping screens has also been investigated during the tests. Actually, the inherent viscous damping of the water is usually much less than the optimal damping that results in optimal performance of the TLD. The inclusion of the damping screens significantly increases the damping ratio and energy dissipation of the water sloshing, thus improving the performance of the TLD. For these scenarios, two damping screens are installed inside the tank at $1/3L$ and $2/3L$ positions, respectively, where L is the length of the tank. The size of each mesh in the screen is 2.2 cm × 2.2 cm.

3. Analytical model to capture TLD-structure interaction

A nonlinear model has been established in [38] for rotating wind turbine blade installed with a TLD. The sloshing motion of the liquid inside the tank was described in a rotating local coordinate system that is fixed to the tank, where the rotation of this coordinate system is due to the rigid-body rotation of the rotor and the elastic rotational deformation of the blade. Modal expansion technique was used for modeling the sloshing of the liquid under gravity, the angular acceleration, the Coriolis acceleration and the centripetal acceleration. Modal expansion was carried out directly on the velocity field of the liquid rather than the velocity potential [20–22] because the Coriolis acceleration renders the potential flow theory invalid even for inviscid fluid flow.

For the present case where the TLD is installed at the top of the wind turbine tower, either the methods proposed in [20–22] or in [38] can be employed to model the TLD-structure interaction (actually they are equivalent). Some of the simpler models [16,17] could also be used although the nonlinear behavior of the liquid sloshing cannot be well captured. In this paper, the theoretical model proposed in [38], which can be generalized to any local coordinate system, has been used with slight modifications. Since no rigid-body rotation takes place for the tower, the rotation of the local coordinate system (for describing the sloshing motion of the liquid) is now only due to the elastic rotational deformation at the tower top. This modified theoretical model is briefly described in the following, and detailed formulation of the coupled nonlinear equations of motion can be found in [38].

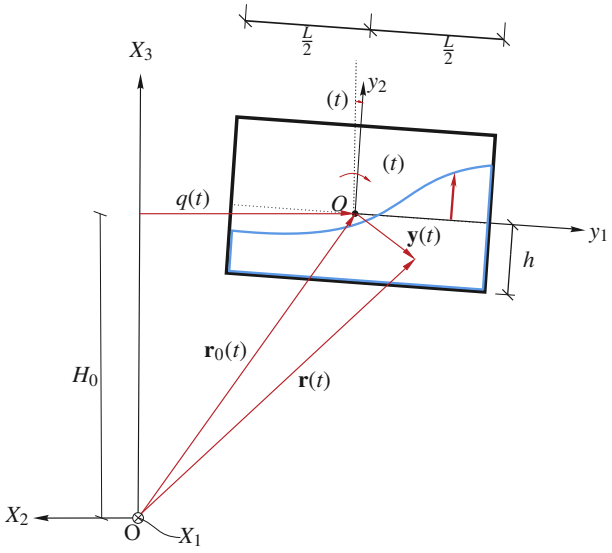

Fig. 6. Modeling of the TLD.

3.1. Modal expansion technique for the sloshing problem

As shown in Fig. 6, the TLD is assumed to be mounted at the top of the wind turbine tower (with the height of H_0), and the elastic displacement and elastic rotation at this position are given by

$$\left.\begin{aligned} q(t) &= -q_8(t) \\ \varphi(t) &= -q_9(t) \end{aligned}\right\} \tag{3}$$

where $q_8(t)$ and $q_9(t)$ are the 8th and 9th degree of freedom of the 13-DOF model as defined in Fig. 3.

The motion of the fluid relative to the tank is described in the local (y_1, y_2, y_3)-coordinate system fixed to the damper with its origin O' placed at the center of the mean water level (MWL). The free surface is defined by a single variable of the surface elevation $\eta(y_1, t)$ measured from the mean water level. Hence, overturning waves, slamming or breaking waves are not covered by this theory. The equations of motion of the fluids are described by the following boundary value problem [38]

$$\left.\begin{aligned} &\rho\left(\tfrac{\partial}{\partial t}\mathbf{v}(\mathbf{y},t) + (\mathbf{v}(\mathbf{y},t)\cdot\nabla)\mathbf{v}(\mathbf{y},t)\right) + c\mathbf{v}(\mathbf{y},t) + \rho\ddot{\mathbf{r}}_0(t) + \rho\dot{\boldsymbol{\omega}}(t)\times(\mathbf{r}_0(t)+\mathbf{y}) + \\ &2\rho\boldsymbol{\omega}(t)\times(\dot{\mathbf{r}}_0(t)+\mathbf{v}(\mathbf{y},t)) + \rho\boldsymbol{\omega}(t)\times(\boldsymbol{\omega}(t)\times(\mathbf{r}_0(t)+\mathbf{y})) = -\nabla p(\mathbf{y},t) + \rho\mathbf{g} \quad , \quad \mathbf{y}\in V(t) \\ &\nabla\cdot\mathbf{v}(\mathbf{y},t) = 0 \quad , \quad \mathbf{y}\in V(t) \\ &\mathbf{v}(\mathbf{y},t)\cdot\mathbf{n}(\mathbf{y}) = 0 \quad , \quad \mathbf{y}\in A_1(t) \\ &p(\mathbf{y},t) = 0 \quad , \quad \mathbf{y}\in A_2(t) \\ &v_2(\mathbf{y},t) = \tfrac{\partial\eta(y_1,y_3,t)}{\partial t} + v_1(\mathbf{y},t)\tfrac{\partial\eta(y_1,y_3,t)}{\partial y_1} + v_3(\mathbf{y},t)\tfrac{\partial\eta(y_1,y_3,t)}{\partial y_3} \quad , \quad \mathbf{y}\in A_2(t) \end{aligned}\right\} \tag{4}$$

The 1st equation in Eq. (4) represents the momentum equation in (y_1, y_2, y_3)-coordinate system. The 2nd equations indicates the mass conservation and incompressibility of the fluid. The boundary condition $\mathbf{v}(\mathbf{y},t)\cdot\mathbf{n}(\mathbf{y}) = 0$ at $A_1(t)$ specifies that the velocity component of the fluid in the outward direction must be zero, where $\mathbf{n}(\mathbf{y})$ is the unit normal vector at $A_1(t)$. At the free surface $A_2(t)$, the pressure above atmospheric pressure $p(\mathbf{y},t)$ must vanish. Further, a fluid particle at the free surface must remain there at all time, which is specified by the other boundary condition at $A_2(t)$.

ρ is the mass density of the fluid, $\mathbf{v}(\mathbf{y},t)$ is the fluid velocity vector relative to the (y_1, y_2, y_3)-coordinate system, $p(\mathbf{y},t)$ is the pressure in the fluid above atmospheric pressure, $\mathbf{g}$ denotes the

acceleration vector due to gravity, $\mathbf{r}_0(t)$ is the position of the origin O' relative to the origin O, and $\mathbf{y}$ and $\mathbf{r}(t)$ denote the position vector of the fluid particle relative to the origins O' and O. $\boldsymbol{\omega}(t)$ and $\dot{\boldsymbol{\omega}}(t)$ indicate the angular rotation vector and angular acceleration vector of the (y_1,y_2,y_3)-coordinate system relative to the (X_1,X_2,X_3)-coordinate system. All the components of the vectors entering Eq. (4) will be indicated in the (y_1,y_2,y_3)-coordinate system, in which the components of $\mathbf{g}$ become time-dependent. Due to the assumed incompressibility, the volume of the fluid is constant in time. However, the shape as specified by the surface elevation $\eta(y_1,y_3,t)$ is changing with time. Therefore, the domain $V(t)$ occupied by the fluid, the wet part of the boundary $A_1(t)$, and the free surface $A_2(t)$ will be time varying as well.

The viscous component in the Navier-Stokes has been omitted in Eq. (4). In principle, energy dissipations in the TLD arise from the fluid viscosity present primarily in the boundary layer, and from the inclusion of flow restricting devices such as damping screens that introduce turbulence in the fluid. In Eq. (4), both of these dissipation mechanisms are accounted for by the term $c\mathbf{v}(\mathbf{y},t)$, which consequently is considered as an approximate equivalent linear damping mechanism. The positive constant c is the linear damping coefficient. One of the aims of this study is also to validate this modeling approach through the tests.

We shall assume that the flow is essential 2-dimensional and takes place in the (y_1,y_2)-plane. This is because the width B of the tank in the y_3-direction is small compared to the length L in the y_1-direction and the mean water height h. As a consequence the flow is independent of the y_3-coordinate.

Next, a weak form of the boundary value problem can be obtained by the Galerkin variational method, where the modal expansions of the velocity field $\mathbf{v}(\mathbf{y},t)$ and its virtual variation $\delta\mathbf{v}(\mathbf{y})$ are expressed as:

$$\left.\begin{aligned}\mathbf{v}(y_1,y_2,t) &= \sum_{i=1}^{N} r_i(t)\mathbf{V}_i(y_1,y_2) \quad , \ \mathbf{y}\in V(t)\\ \delta\mathbf{v}(y_1,y_2) &= \sum_{i=1}^{N} \delta r_i \mathbf{V}_i(y_1,y_2) \quad , \ \mathbf{y}\in V(t)\end{aligned}\right\} \tag{5}$$

where $r_i(t)$ and δr_i denote the generalized coordinates of the velocity field and the variational field. The shape functions $\mathbf{V}_i(y_1,y_2)$ are not required to fulfill any mechanical boundary conditions on the free surface. However, they need to have zero divergence and to fulfill vanishing kinematical boundary conditions on the side walls.

In this respect, the eigenmodes of standing waves in linear wave theory have been used as shape functions:

$$\mathbf{V}_i(\mathbf{y}) = \begin{bmatrix} -\sin\left(k_i\left(y_1+\frac{L}{2}\right)\right)\cosh(k_i(y_2+h)) \\ \cos\left(k_i\left(y_1+\frac{L}{2}\right)\right)\sinh(k_i(y_2+h)) \\ 0 \end{bmatrix},$$
$$(y_1,y_2) = \left[-\frac{L}{2},\frac{L}{2}\right]\times[-h,\eta(y_1,t)] \tag{6}$$

where $k_i = i\frac{\pi}{L}$ is the wave number. The angular frequency of the ith sloshing mode is given by:

$$\omega_i^2 = gk_i\tanh(k_ih) \tag{7}$$

The boundary condition on the free surface is discretized in a similar manner. The surface elevation $\eta(y_1,t)$ and its virtual variation $\delta\eta(y_1)$ are given by the expansions:

$$\left.\begin{aligned}\eta(y_1,t) &= \sum_{i=1}^{N} s_i(t)\cos\left(k_i\left(y_1+\tfrac{L}{2}\right)\right)\\ \delta\eta(y_1) &= \sum_{i=1}^{N}\delta s_i\cos\left(k_i\left(y_1+\tfrac{L}{2}\right)\right)\end{aligned}\right\} \tag{8}$$

where $s_i(t)$ and δs_i denote the generalized coordinates of $\eta(y_1,t)$ and $\delta\eta(y_1)$. The selected shape functions in Eq. (8) is motivated by the linear wave theory, where the free surface condition reduces to $v_2(y_1,0,t) = \frac{\partial}{\partial t}\eta(y_1,t)$. Hence, the distribution with y_1 for each shape function in Eq. (8) should be pairwise proportional to its counterpart in Eq. (6).

Further, coupled nonlinear differential equations for $r_i(t)$ and $s_i(t)$ can be obtained by substituting Eqs. (5), (6) and (8) into the weak formulation of the boundary value problem [38]. The linear viscous damping in the field equation Eq. (4) provides a modal damping matrix with the components $c_{ij} = \frac{c}{\rho}m_{ij}$ in the discretized equations, where m_{ij} signifies the components of the modal mass matrix given by

$$m_{ij} = B\int_{-h}^{0}\int_{-L/2}^{L/2}\rho\mathbf{V}_i(y_1,y_2)\cdot\mathbf{V}_j(y_1,y_2)dy_1dy_2 \tag{9}$$

Finally, the damping coefficient c in Eq. (4) is prescribed in the form

$$c = \xi\rho\omega_1 \tag{10}$$

where ω_1 is the fundamental eigenfrequency given by Eq. (7) and ξ is a non-dimensional damping parameter, which will be used as a measure of the total energy dissipation (both the viscous effect and the damping screens) in this theoretical model.

3.2. The sloshing force

As shown in Fig. 7, $\mathbf{f}_c(t)$ with the non-vanishing moving frame components $f_{c,1}(t)$ and $f_{c,2}(t)$, denotes the external reaction force vector on the liquid due to the pressure $p(\mathbf{y},t)$ from inner side of the tank. This force vector, when transferred to the primary structure, represents the control force for lateral tower vibrations. The analytical expression of $\mathbf{f}_c(t)$ can be obtained by integrating the pressure $p(\mathbf{y},t)$ over inner surfaces of the tank, in combination with the divergence theorem [38]. This force vector is dependent on the state variables $s_i(t)$ through the time-varying fluid domain $V(t)$.

4. Test results and analysis

Considering the size of the manufactured TLD, the suitable ratings of wind turbine could be 2 MW and 3 MW, and both of them have been considered in establishing the Matlab/Simulink model. To obtain data of these two configurations, a classical upscaling/downscaling method [39] has been used on the widely used National Renewable Energy Laboratory (NREL) 5-MW reference turbine [40]. The resulting system parameters of the two turbines are provided in Table 1. The inherent structural damping 1% for the

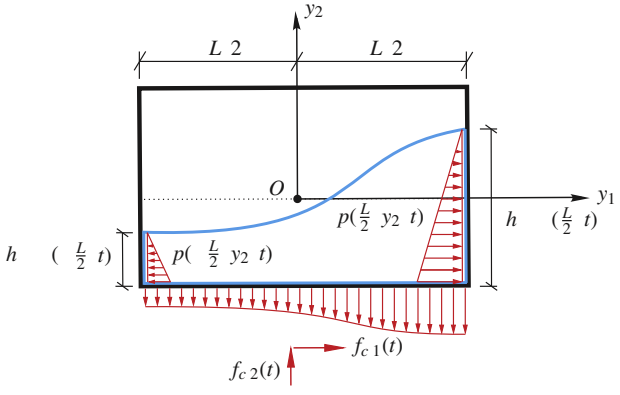

Fig. 7. Pressure distribution on inner surfaces of the TLD tank.

Table 1
Parameters of the two wind turbines used in the Simulink model.

Parameter	2 MW	3 MW
Rotor rotational speed (rad/s)	2.00	1.63
Blade radius (m)	40	49
Blade mass (kg)	4488.0	8244.8
Blade structural damping ratio (–)	0.005	0.005
Rotor moment of inertia (kg m^2)	3.768×10^6	1.039×10^7
Nacelle + hub mass (kg)	7.508×10^4	1.379×10^5
Hub height (m)	55.4	67.9
Tower mass (kg)	8.790×10^4	1.615×10^5
Tower structural damping ratio (–)	0.01	0.01
First lateral tower frequency (rad/s)	3.37	2.75

tower and 0.5% for the blades are chosen in accordance with the values used for the NREL 5-MW turbine (1% for the tower and 0.48% for the blade) [40].

Eq. (7) is used for tuning the TLD (by changing the mean water lever h), so that the first sloshing frequency is close to the first lateral tower frequency shown in Table 1. For each wind turbine model, tests were undertaken for three different tuning ratios (ratio between the first sloshing frequency to the first lateral tower frequency) of the TLD and using three different turbulent wind loads. Moreover, cases of the TLD with and without damping screens were both evaluated. Therefore, in total 36 ($= 2 \times 3 \times 3 \times 2$) real-time hybrid tests were conducted, and the duration for each test was set to be 5 min.

4.1. Delay compensation

The developed compensation method in [25] predicts the displacement of the actuator after the actuator delay δt from the present time by extrapolating an nth-order polynomial function based on the target (present) displacement and n previous calculated displacements ($\delta t \times i$ units of time ago, $i = 1, 2, \ldots, n$). Therefore, the predicted displacement is δt time ahead of the target counterpart.

By sending a sinusoidal signal to the actuator, the delay time δt was identified as 15 ms for the system in this study (it depends both on the actuator and the physical substructure). This delay time was used in the compensation technique for predicting (extrapolating) the actuator displacement during all tests. Fig. 8 (a) shows the results of one test case without delay compensation, where the solid line is the displacement calculated by the computer (target displacement) and dashed line is the displacement command sent to the actuator by the controller. They are identical when no compensation is applied. The dotted line is the measured displacement (feedback displacement from the actuator), which is observed to be about 15 ms delayed comparing with the target displacement. Fig. 8(b) shows the corresponding results for the same load case with the delay compensation technique applied. The black dashed line is the predicted (extrapolated using the polynomial function) displacement, which is now about 15 ms ahead of the target displacement. By applying this predicted value as a command signal to the actuator, the resulting displacement becomes almost identical to the target one, since the command signal is delayed by the actuator.

4.2. Control effect of the TLD on tower vibrations

For each wind turbine model, three different wind fields (with different combinations of the mean wind speed V_0 and the turbulence intensity I) have been applied.

Table 2 shows the response reduction of lateral tower vibrations of the 2 MW wind turbine by the TLD. The water level of TLD varies from 46.74 cm to 64.80 cm corresponding to three values of tuning ratio η (0.95, 1.0, 1.05). With fixed size of the tank, the resulting water mass is only dependent on the water level, and it varies from 532.23 kg to 737.88 kg. Reductions of both the standard deviation (STD) and the maximum value of the tower top displacement are presented. For performance evaluation of the TLD, the STD reduction is clearly a better index since it indicates the overall reduction of the response and thus the fatigue life improvement. The peak reduction is less representative since the peak response occurs only at a certain instant of time and is more stochastic in nature. Actually, it is known that fatigue damage in wind turbines is

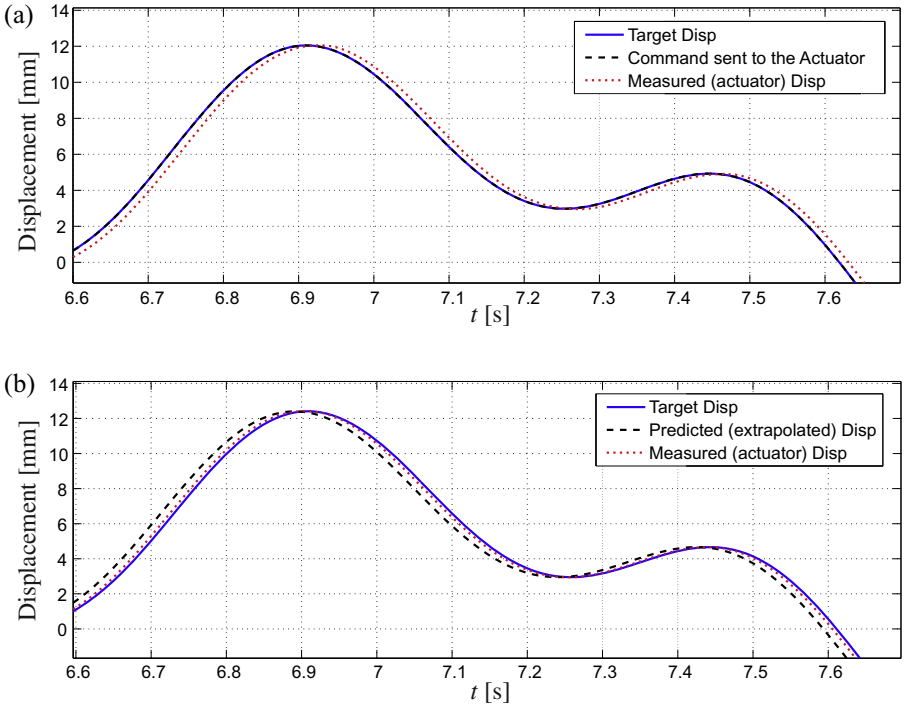

Fig. 8. Accuracy of the applied delay compensation technique. (a) Without compensation; (b) with compensation.

Table 2
Response reduction of lateral tower vibrations of the 2 MW wind turbine by TLDs with different configurations.

Wind loads	Tuning ratio	Screen	Water level (cm)	Water mass (kg)	STD reduction (%)	Peak reduction (%)
$V_0 = 12$ m/s, $I = 0.08$	$\eta = 1.0$	No	54.61	621.84	40	34
		Yes	54.61	621.84	52	48
	$\eta = 0.95$	No	46.74	532.23	28	35
		Yes	46.74	532.23	31	39
	$\eta = 1.05$	No	64.80	737.88	42	15
		Yes	64.80	737.88	50	25
$V_0 = 12$ m/s, $I = 0.1$	$\eta = 1.0$	No	54.61	621.84	44	33
		Yes	54.61	621.84	53	49
	$\eta = 0.95$	No	46.74	532.23	29	37
		Yes	46.74	532.23	33	41
	$\eta = 1.05$	No	64.80	737.88	37	10
		Yes	64.80	737.88	50	27
$V_0 = 8$ m/s, $I = 0.1$	$\eta = 1.0$	No	54.61	621.84	20	9
		Yes	54.61	621.84	32	13
	$\eta = 0.95$	No	46.74	532.23	22	15
		Yes	46.74	532.23	26	16
	$\eta = 1.05$	No	64.80	737.88	9	2
		Yes	64.80	737.88	25	21

related to effect of turbulence which is represented by the power spectral density functions (PSDFs) of the relevant response quantities [41]. The PSDF in turn is related to the STD of the response, implying that STD is representative of the fatigue damage.

From Table 2, there are three observations to be emphasized:

(i) For all load cases and all configurations, the TLD is effective in reducing the standard deviations and peak values of the tower top displacement. Hence, the dynamic response and fatigue life of the 2 MW wind turbine tower can be successfully improved by the TLD designed in this study.
(ii) The inclusion of damping screens in the TLD significantly improves the control performance of the damper, for all wind loads scenarios and all tuning ratios. Especially for the case of $V_0 = 8$ m/s and $\eta = 1.05$, both the STD and peak reductions (negligible reductions before damping screens included) have been significantly increased when damping screens are included. By equipping two damping screens, more energies are dissipated during sloshing and the bandwidth of TLD becomes broader.
(iii) For the TLD without damping screens, the optimal tuning ratio depends on the mean wind speed and the turbulence intensity. For cases with damping screens, the optimal tuning ratio is always 1.0 when STD reductions are used as index. The same conclusion can be drawn from the peak reductions, except for the case of $V_0 = 8$ m/s where the largest peak reduction is achieved when $\eta = 1.05$. Acceptable control performance of the TLD can be obtained for all three tuning ratios considered here, but in general the best performance is achieved for all wind load cases when $\eta = 1.0$ with damping screens equipped.

Fig. 9 shows the control effect of the TLD on tower vibrations of the 2 MW wind turbine in both time and frequency domains, for the case of $V_0 = 12$ m/s, $I = 0.08, \eta = 1.0$. Fig. 9(a) and (b) correspond to the TLD without and with damping screens, respectively. For both scenarios, the tower top displacement $q_8(t)$ is significantly reduced by the TLD, while the inclusion of damping screens further improves the reduction effect as shown in Fig. 9(b). From the Fourier amplitude of $q_8(t)$ a clear peak corresponding to the first lateral tower frequency (3.37 rad/s) is observed due to very low aerodynamic damping in this mode. This peak is effectively suppressed by the damper, and is almost totally eliminated when damping screens are included in the TLD. Moreover, in the frequency domain two very small peaks (around 9 rad/s and 13 rad/s) can also been observed, resulting from the coupling between the lateral tower vibration to the edgewise blade vibrations. The TLD has no effect on these two peaks.

Table 3 shows the performance of the TLD on the 3 MW wind turbine. Comparing with Table 2, slightly different results have been obtained, with the following observations to be highlighted:

(i) The overall control effect of the TLD is slightly worse comparing with the results in Table 2. Since the tower frequency of the 3 MW wind turbine is lowered to 2.75 rad/s, the mean water level (for tuning the sloshing frequency) and thus the water mass of the TLD are reduced, resulting in smaller mass ratio of the damper.
(ii) For all wind load cases, when $\eta = 1.05$ and no screens are used, the peak responses are increased by installation of TLD. This might be due to the beating phenomenon arising out of tuning, where during certain period of time a fraction of the energy absorbed by the TLD is transferred back in phase with the structural motion, rather than dissipating the energy. By including damping screens, energy is dissipated through damping and this problem is eliminated. Researchers in the past have also shown that optimal tuning ratios are generally not greater than one [42–44].
(iii) For some cases (such as $V_0 = 12$ m/s, $I = 0.1$, $\eta = 0.95$), the inclusion of damping screens even deteriorates the performance of the TLD. This might be attributed to the increased nonlinear effect when the water height is shallow in the tank. Due to the increased nonlinearity, the performance of the TLD becomes more irregular in comparison with the results in Table 2.
(iv) For all wind load cases the best performance of the TLD is always obtained when the tuning ratio is 1 and damping screens are equipped. This turns out to be the optimal design of the TLD for both 2 MW and 3 MW wind turbines.

Fig. 10 shows the performance of the TLD on the 3 MW wind turbine in both time and frequency domains, for the case of $V_0 = 12$ m/s, $I = 0.1, \eta = 1.0$. Again, Fig. 10(a) and (b) correspond to the TLD without and with damping screens, respectively. It is observed that the equipped damping screens effectively improve the control effect of the TLD, and STD reduction calculated from the 5-min time histories is increased from 28% to 40%. The spectrum peak corresponding to the first lateral tower frequency (2.74 rad/s) is reduced by half in Fig. 10(a) and by 1/3 in Fig. 10 (b) using the TLD with damping screens.

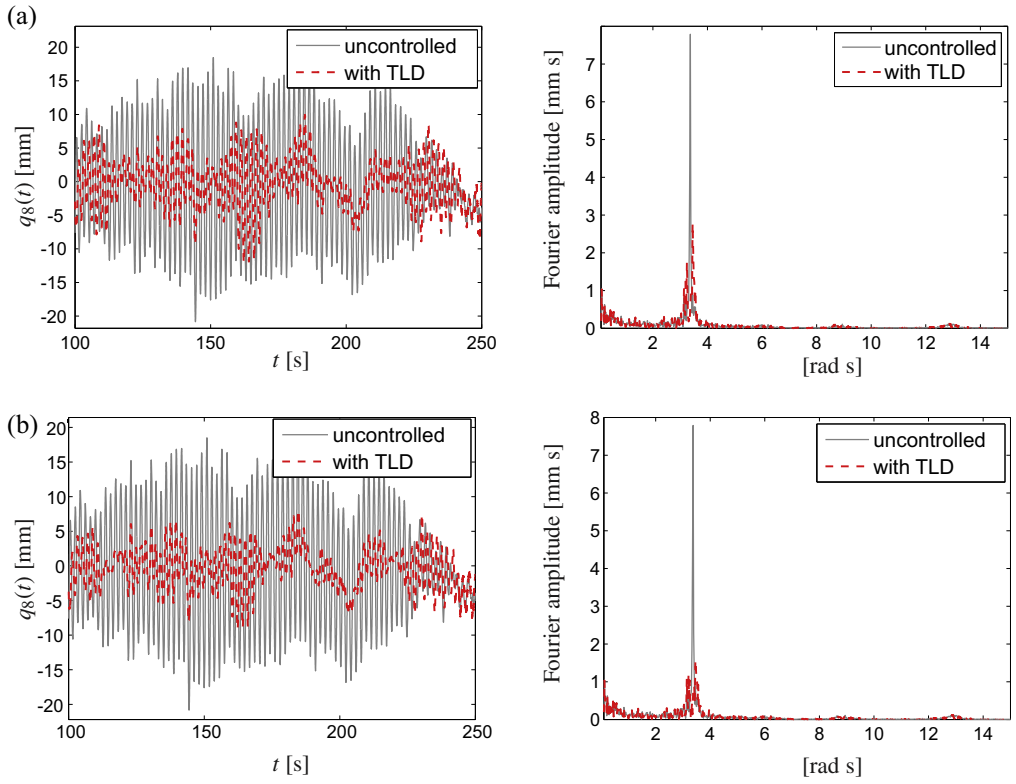

Fig. 9. Control effect of the TLD on tower vibrations of the 2 MW wind turbine, tuning ratio = 1, $V_0 = 12$ m/s, $I = 0.08$. (a) Without damping screens, (b) with damping screens.

Table 3
Response reduction of lateral tower vibrations of the 3 MW wind turbine by TLDs with different configurations.

Wind loads	Tuning ratio	Screen	Water level (cm)	Water mass (kg)	STD reduction (%)	Peak reduction (%)
$V_0 = 12$ m/s, $I = 0.08$	$\eta = 1.0$	No	31.64	360.28	28	18
		Yes	31.64	360.28	40	30
	$\eta = 0.95$	No	28.08	319.75	28	27
		Yes	28.08	319.75	19	5
	$\eta = 1.05$	No	35.62	405.60	18	−3
		Yes	35.62	405.60	28	13
$V_0 = 12$ m/s, $I = 0.1$	$\eta = 1.0$	No	31.64	360.28	29	26
		Yes	31.64	360.28	44	30
	$\eta = 0.95$	No	28.08	319.75	33	25
		Yes	28.08	319.75	22	10
	$\eta = 1.05$	No	35.62	405.60	14	−5
		Yes	35.62	405.60	26	10
$V_0 = 8$ m/s, $I = 0.1$	$\eta = 1.0$	No	31.64	360.28	8	5
		Yes	31.64	360.28	30	34
	$\eta = 0.95$	No	28.08	319.75	10	5
		Yes	28.08	319.75	13	5
	$\eta = 1.05$	No	35.62	405.60	7	−5
		Yes	35.62	405.60	19	12

4.3. Measured wave heights and control forces

Fig. 11 compares the measured wave heights at the left end wall of the TLD with and without damping screens for the 2 MW wind turbine, where $V_0 = 12$ m/s, $I = 0.08, \eta = 1.0$. From the time histories in Fig. 11(a), it is observed that the water sloshes in a similar trend for both cases, but much larger amplitude of the wave height is observed when there are no damping screens. Obviously the inclusion of damping screens leads to increased energy dissipation during sloshing and thus mitigated motion of the water. Moreover, for TLD with damping screens, the time history of the wave height near the tank wall turns out to be more symmetric about zero axis, implying a dominating 1st sloshing mode.

The corresponding Fourier amplitude of the wave heights is illustrated in Fig. 11(b). For the case without damping screens, several spectral peaks can be clearly observed, of which the most significant one corresponds to the 1st sloshing mode. From Eq. (7), theoretical values (linear wave theory) of the 2nd, 3rd and 5th sloshing frequencies are calculated as 5.49 rad/s, 6.89 rad/s and 8.93 rad/s, respectively. These three sloshing modes are also presented in Fig. 11(b), implying significant contributions from higher modes in the sloshing of the liquid. Further, it is interesting to observe two other peaks at about 6.7 rad/s and 10.1 rad/s, corresponding to 2 times and 3 times the first sloshing frequency ω_1, respectively. This is due to the inherent nonlinear characteristics of the sloshing system, and higher-harmonics (multiples of the first

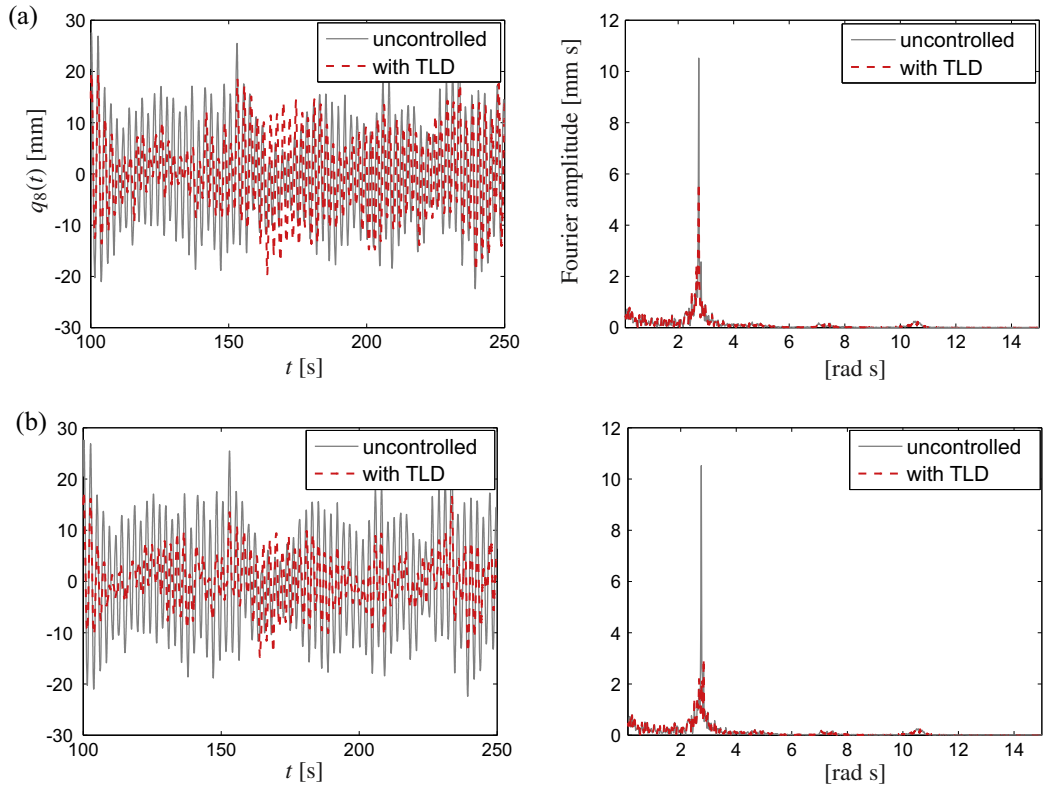

Fig. 10. Control effect of the TLD on tower vibrations of the 3 MW wind turbine, tuning ratio = 1, $V_0 = 12$ m/s, $I = 0.1$. (a) Without damping screens, (b) with damping screens.

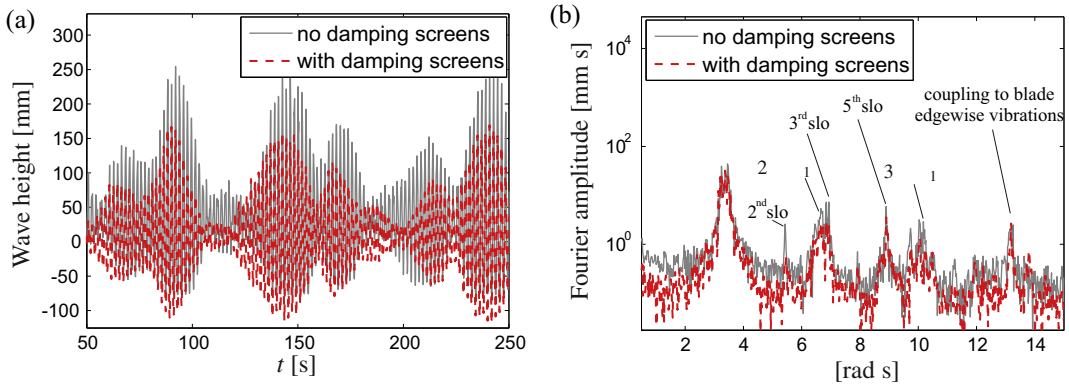

Fig. 11. Measured wave heights at the left end wall of the tank, 2 MW wind turbine, tuning ratio = 1, $V_0 = 12$ m/s, $I = 0.08$. (a) Time histories, (b) Fourier amplitude in semi-logarithmic chart.

frequency) are presented in the liquid response. On the other hand, for the case with damping screens, all the above mentioned peaks are effectively suppressed, resulting in a dominated peak of the first sloshing frequency (although this peak is suppressed as well). This again explains the more symmetric time history of the wave height about the zero axis in Fig. 11(a). Finally, in both cases a peak at about 13 rad/s is presented with the same magnitude. As earlier remarked, this peak results from the coupling of the tower with blade edgewise vibrations, and the inclusion of damping screens has no influence on it.

In connection to Figs. 11 and 12 compares the measured (by the actuator) control force (sloshing force) for cases with and without damping screens. From Fig. 12(a) it is seen that the insertion of damping screens reduces the magnitude of the control force, even though the control effect of the TLD is improved as shown in Fig. 9. The corresponding Fourier amplitude in Fig. 12(b) shows a dominating peak of the first sloshing mode as expected. Two small peaks at the 3rd and 5th sloshing angular frequencies are also observed for the case without damping screens. The 2nd sloshing mode is totally gone because it has no contribution to the resulting control force. Moreover, peaks of $2 \times \omega_1$ and $3 \times \omega_1$ in Fig. 11(b) are also filtered out since the force is the result of integrating liquid pressures over inner walls of the tank. By including damping screens, peaks of the 3rd and 5th sloshing modes are further eliminated, leaving only the fundamental peak and the peak due to the coupling effect with the blade vibrations.

For the 3 MW wind turbine with a lower tower frequency, the water depth (for tuning the damper) in the tank is more shallow and nonlinear effect of the sloshing system becomes more pronounced.

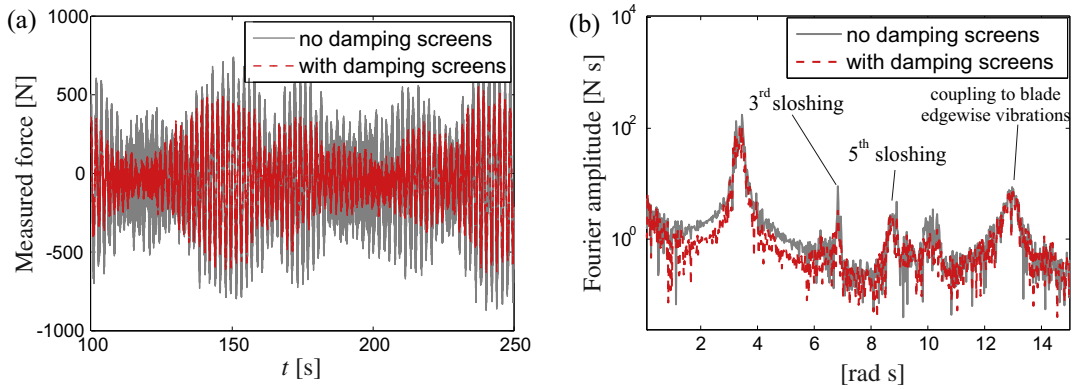

Fig. 12. Measured control force from the TLD, 2 MW wind turbine, tuning ratio = 1, $V_0 = 12$ m/s, $I = 0.08$. (a) Time histories, (b) Fourier amplitude in semi-logarithmic chart.

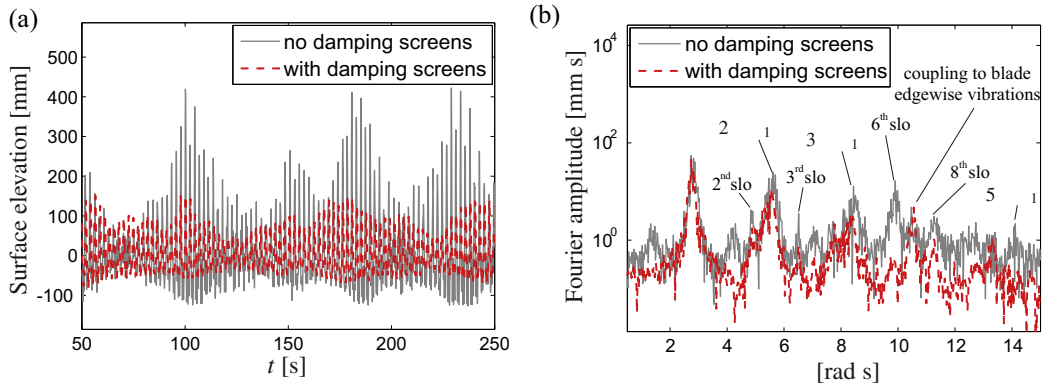

Fig. 13. Measured wave heights at the left end wall of the tank, 3 MW wind turbine, tuning ratio = 1, $V_0 = 12$ m/s, $I = 0.08$. (a) Time histories, (b) Fourier amplitude in semi-logarithmic chart.

Fig. 13 illustrates the measured wave height at the left end wall for the 3 MW wind turbine, with $V_0 = 12$ m/s, $I = 0.08, \eta = 1.0$. Very drastic motion of the liquid is shown in Fig. 13(a) for the case without damping screens. Actually, wave breaking was also observed during the test. Again the inclusion of damping screens mitigate the liquid motion effectively. From Fig. 13(b), peaks corresponding to the 2nd sloshing, the 3rd sloshing, the 6th sloshing, the 8th sloshing are observed together with $2 \times \omega_1$ and $3 \times \omega_1$ peaks. By inserting damping screens, all peaks corresponding to the higher sloshing modes are almost totally eliminated, but the $2 \times \omega_1$ and $3 \times \omega_1$ peaks are still visible (although suppressed).

Correspondingly, Fig. 14 shows the measured control force in both time and frequency domains. Observations similar to those in Fig. 12 can be made, except that the frequency components of the control force (without damping screens) turn out to be the dominating 1st sloshing, the 3rd sloshing, together with $3 \times \omega_1$ and $5 \times \omega_1$ due to nonlinear interactions. This again shows the more pronounced nonlinear effect of the relatively shallow water for the 3 MW wind turbine, since peaks corresponding to nonlinear interactions are totally eliminated in Fig. 12(b) for the 2 MW wind turbine.

For Figs. 11–14, some further remarks are made as follows. Although the liquid motion contains a lot of frequency components including both the higher sloshing modes and the nonlinear interaction effects, the resulting control force filters out most of the high frequency components. Applied to the main structure, the

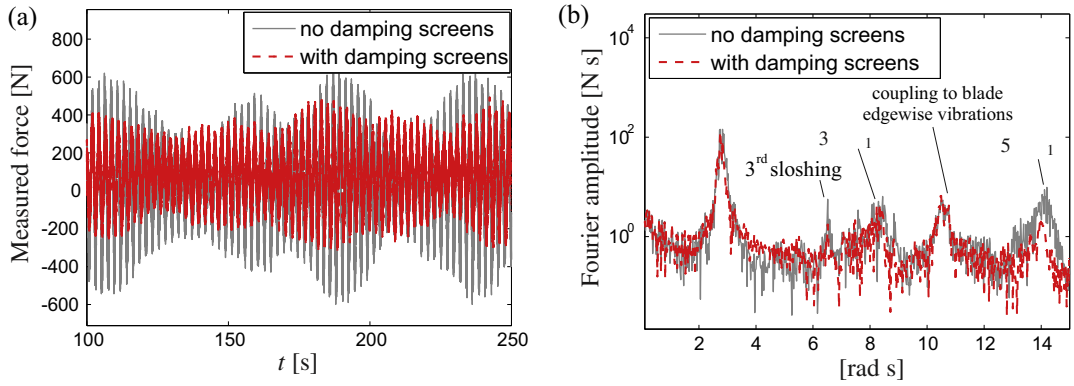

Fig. 14. Measured control force from the TLD, 3 MW wind turbine, tuning ratio = 1, $V_0 = 12$ m/s, $I = 0.1$. (a) Time histories, (b) Fourier amplitude in semi-logarithmic chart.

remaind small amounts of high frequency components are further filtered out by the structure. Further, better control effect is achieved when the resulting control force is dominated by the first sloshing frequency without high frequency components.

4.4. Comparison of results from RTHT and analytical model

Modal expansions to three sloshing modes ($N = 3$) in Eqs. (5) and (8) have been carried out in the numerical simulations using the analytical model. Two different values of the non-dimensional damping parameter ξ, corresponding to different total energy dissipations, are used in the model for cases with and without damping screens. To determine the value of ξ in each case, try-and-error method has been used by trying different values of ξ in the analytical model. The best estimation of ξ is obtained in order that the corresponding result from the model fits best with the experimental result.

Fig. 15 shows the comparison of the controlled tower top displacements obtained by RTHT and the analytical model for the 2 MW wind turbine, where $V_0 = 12$ m/s, $I = 0.08, \eta = 1.0$. By setting the damping parameter ξ to be 0.004, the result from the analytical model agrees very well with the test result as shown in Fig. 15(a). Acceptable agreement between the experimental and analytical results is also obtained for the case with damping screens by choosing the value of ξ to be 0.02.

Fig. 16 shows a similar comparison for the 2 MW wind turbine under the load scenario of $V_0 = 8$ m/s, $I = 0.1, \eta = 1.0$. Again, there is a good agreement between the test and analytical results for the case without damping screens. The analytical result fits slightly worse with the test result for the case with damping screens. This is reasonable because in fact the inclusion of damping screens not only increases energy dissipation but also introduces nonlinear interactions between the liquid and the screens, which is not accounted for by the present analytical model.

As for the 3 MW wind turbine, comparison of the results obtained by RTHT and the analytical model are shown in Fig. 17, where $V_0 = 12$ m/s, $I = 0.1, \eta = 1.0$. ξ is set to be 0.005 and 0.03 in the analytical model for cases without and with damping screens, respectively. Good agreement between the experimental and analytical results is obtained. Fig. 18 shows the comparison under the load scenario of $V_0 = 8$ m/s, $I = 0.1, \eta = 1.0$. Similar observations are obtained, where the agreement is worse for the case with damping screens. Further, for TLDs used in the 3 MW turbine, larger values of ξ have been used in the analytical model comparing with its 2 MW counterpart, implying larger energy dissipations of the shallow water TLD due to nonlinear interactions and wave breaking.

To get deeper understanding of the overall energy dissipation in relation with the screen elements, and to facilitate the analysis and design of the TLD in practical applications, it's preferable that the empirical relation between the mesh size of the screen elements and the damping parameter ξ can be established. Recently, we have carried out a series of real-time hybrid testing on the same TLD, but with different mesh sizes of the screen elements. With the comprehensive test data obtained, the empirical relation (expression) is expected to be established, from which the value of ξ can be determined immediately when given the mesh sizes of the screen elements.

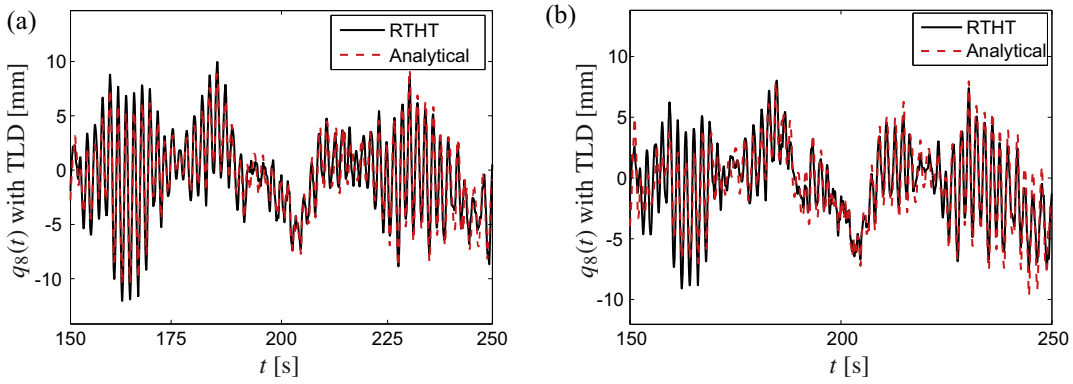

Fig. 15. Comparison of the controlled tower displacements obtained by RTHT and analytical model, 2 MW wind turbine, tuning ratio = 1, $V_0 = 12$ m/s, $I = 0.08$. (a) Without damping screens ($\xi = 0.004$ used in the analytical model), (b) with damping screens ($\xi = 0.02$ used in the analytical model).

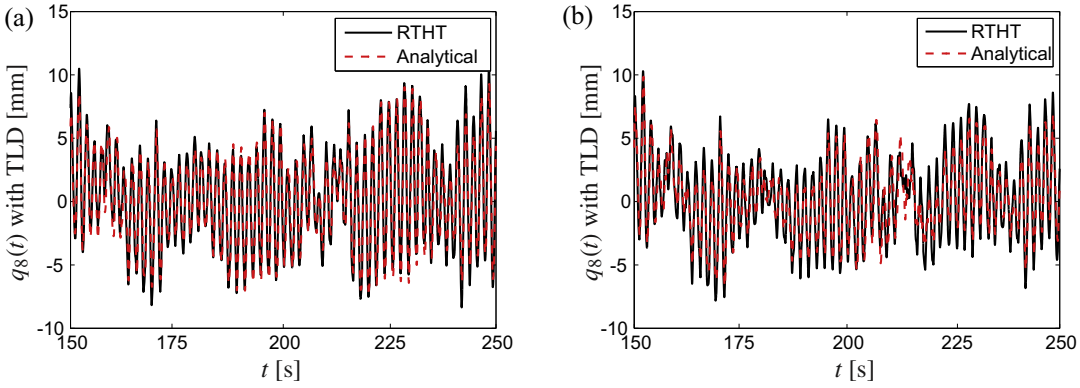

Fig. 16. Comparison of the controlled tower displacements obtained by RTHT and analytical model, 2 MW wind turbine, tuning ratio = 1, $V_0 = 8$ m/s, $I = 0.1$. (a) Without damping screens ($\xi = 0.004$ used in the analytical model), (b) with damping screens ($\xi = 0.015$ used in the analytical model).

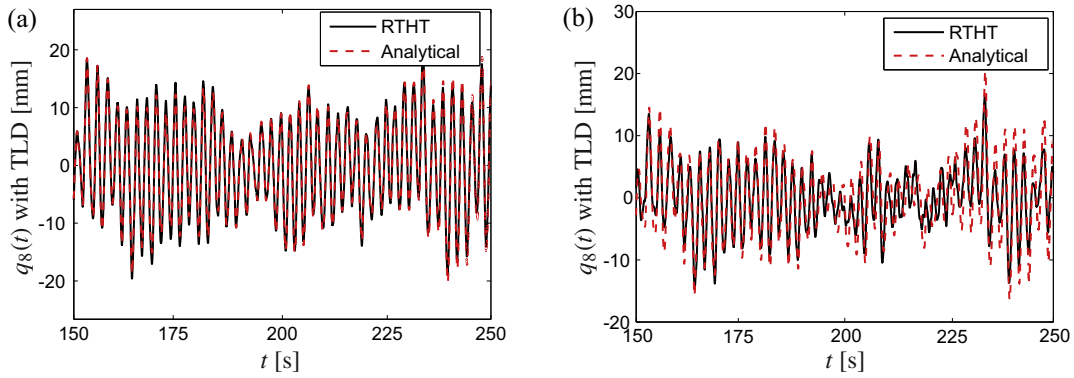

Fig. 17. Comparison of the controlled tower displacements obtained by RTHT and analytical model, 3 MW wind turbine, tuning ratio = 1, $V_0 = 12$ m/s, $I = 0.1$. (a) Without damping screens ($\xi = 0.005$ used in the analytical model), (b) with damping screens ($\xi = 0.03$ used in the analytical model).

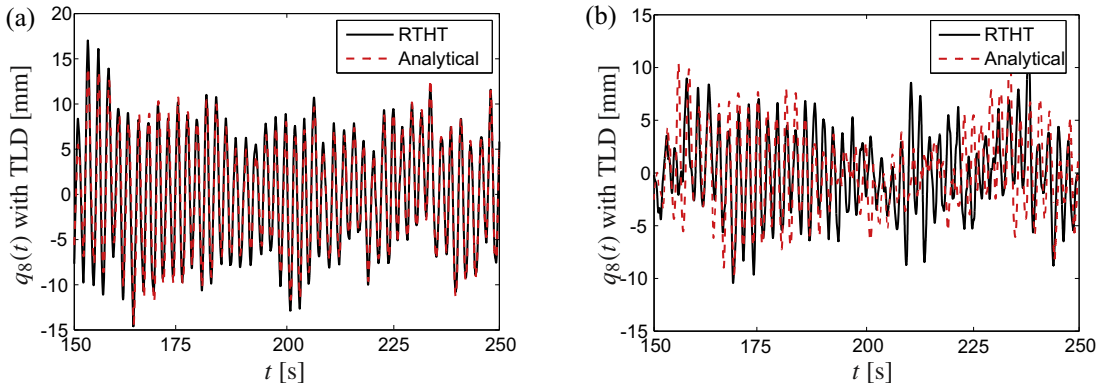

Fig. 18. Comparison of the controlled tower displacements obtained by RTHT and analytical model, 3 MW wind turbine, tuning ratio = 1, $V_0 = 8$ m/s, $I = 0.1$. (a) Without damping screens ($\xi = 0.005$ used in the analytical model), (b) with damping screens ($\xi = 0.04$ used in the analytical model).

5. Conclusions

In this paper, the performance of a full-scale TLD in mitigating lateral tower vibrations of megawatt wind turbines exhibiting some special features has been investigated with the aid of real-time hybrid testing (RTHT) method. During the RTHT, a full-size TLD is tested as the physical substructure while the structural responses of the wind turbine system are numerically calculated using a 13-DOF aeroelastic model in the Matlab/Simulink environment. A compensation technique based on polynomial extrapolation has been applied to compensate for the inherent actuator delay.

Both 3 MW and 2 MW wind turbine models have been established in Matlab/Simulink, and different water levels of the TLD are determined from frequency tuning conditions for the two turbines. The overall control effect of the TLD is slightly worse for the 3 MW wind turbine (with lower tower frequency) due to the reduced mean water level and thus the mass ratio of the damper. Moreover, it is shown from test results that the inclusion of damping screens effectively increases energy dissipation during liquid sloshing and in most cases improves the control performance of the TLD on tower vibrations. For both turbines under all load cases, the best performance of the TLD is always obtained when the tuning ratio is 1.0 and damping screens are equipped. Furthermore, the measured wave height at the left end wall is observed to contain a lot of frequency components including both the higher sloshing modes and the nonlinear interaction effect. The measured control force, on the other hand, filters out most of the high frequency components since the force is the result of integrating liquid pressures over inner walls of the tank. By inserting damping screens, the remaining high frequency components are further mitigated, resulting in a control force that is totally dominated by the first sloshing frequency.

Finally, the RTHT results are compared to the results obtained from an analytical model of the TLD-wind turbine system (based on modal expansion technique). Good agreement between tested and analytical results demonstrates that the proposed analytical method can yield acceptable estimates of the response of wind turbine-TLD system under turbulent wind loads. The comparative results also indicate that the real-time hybrid test method provides an accurate and cost-effective procedure for performing full-scale tests of passive or semi-active dampers.

The wind turbine foundation is modeled as fully fixed in the present study. Although in practice the rocking motion of the foundation has to be reduced as much as possible for wind turbines under normal operational conditions, by means of proper design and construction techniques. The soil-structure interaction may still influence the performance of the damper on controlling tower vibrations, especially the tuning condition of the damper. In future works, investigation on vibration control of wind turbines considering soil-structure interaction may be carried out with the aid of RTHT method.

Acknowledgements

The first author gratefully acknowledge the financial support from the Chinese Scholarship Council under the State Scholarship Fund. The authors would like to acknowledge the contributions of the technical staff (especially Dr. Kevin Ryan and Mr. David McAulay) in the Structures Laboratory at Trinity College Dublin.

References

[1] Hansen MH. Aeroelastic instability problems for wind turbines. Wind Energy 2007;10(6):551–77.
[2] Thomsen K, Petersen JT, Nim E, Øye S, Petersen B. A method for determination of damping for edgewise blade vibrations. Wind Energy 2000;3(4):233–46.
[3] Bir G, Jonkman J. Aeroelastic instabilities of large offshore and onshore wind turbines. In: EAWE 2007 Torque from Wind Conference, Lyngby, Denmark.
[4] Staino A, Basu B, Nielsen SRK. Actuator control of edgewise vibrations in wind turbine blades. J Sound Vib 2012;331(6):1233–56.
[5] Basu B, Zhang Z, Nielsen SRK. Damping of edgewise vibration in wind turbine blades by means of circular liquid dampers. J Sound Vib 2016;19(2):213–26.
[6] Argyriadis K, Hille N. Determination of fatigue loading on a wind turbine with oil damping device. In: Proceedings of the 2004 European Wind Energy Conference & Exhibition, London.
[7] Murtagh PJ, Ghosh A, Basu B, Broderick BM. Passive control of wind turbine vibrations including blade/tower interaction and rotationally sampled turbulence. Wind Energy 2008;11(4):305–17.
[8] Colwell S, Basu B. Tuned liquid column dampers in offshore wind turbines for structural control. Eng Struct 2009;31(2):358–68.
[9] Lackner MA, Rotea MA. Passive structural control of offshore wind turbines. Wind Energy 2011;14(3):373–88.
[10] Zhang ZL, Chen JB, Li J. Theoretical study and experimental verification of vibration control of offshore wind turbines by a ball vibration absorber. Struct Infrastruct Eng 2014;10(8):1087–100.
[11] Fujii K, Tamura Y, Sato T, Wakahara T. Wind-induced vibration of tower and practical applications of tuned sloshing damper. J Wind Eng Ind Aerodynam 1990;33(1–2):263–72.
[12] Chang CC, Gu M. Suppression of vortex-excited vibration of tall buildings using tuned liquid dampers. J Wind Eng Ind Aerodynam 1999;83(1–3):225–37.
[13] Banerji P, Murudi M, Shah AH, Popplewell N. Tuned liquid dampers for controlling earthquake response of structures. Earthq Eng Struct Dynam 2000;29(5):587–602.
[14] Lee SK, Park EC, Min KW, Lee SH, Chung L, Park JH. Real-time hybrid shaking table testing method for the performance evaluation of a tuned liquid damper controlling seismic response of building structures. J Sound Vib 2007;302(3):471–88.
[15] Jin Q, Li X, Sun N, Zhou J, Guan J. Experimental and numerical study on tuned liquid dampers for controlling earthquake response of jacket offshore platform. Mar Struct 2007;20(4):238–54.
[16] Sun LM, Fujino Y, Chaiseri P, Pacheco BM. The properties of tuned liquid dampers using a TMD analogy. Earthq Eng Struct Dynam 1995;24(7):967–76.
[17] Yu JK, Wakahara T, Reed D. A nonlinear numerical model for the tuned liquid damper. Earthq Eng Struct Dynam 1999;28(6):671–86.
[18] Sun LM, Fujino Y. A semi-analytical model for tuned liquid damper (TLD) with wave breaking. J Fluids Struct 1994;8(5):471–88.
[19] Reed D, Yu J, Yeh H, Gardarsson S. Investigation of tuned liquid dampers under large amplitude excitation. J Eng Mech 1998;124(4):405–13.
[20] Faltinsen OM, Regnebakke OF, Lukovsky IA, Timokha AN. Multidimensional model analysis of nonlinear sloshing in a rectangular tank with finite water depth. J Fluid Mech 2000;407:201–34.
[21] Faltinsen OM, Timokha AN. An adaptive multimodal approach to nonlinear sloshing in a rectangular tank. J Fluid Mech 2001;432:167–200.
[22] Love JS, Tait MJ. Nonlinear simulation of a tuned liquid damper with damping screens using a modal expansion technique. J Fluid Struct 2010;26(7–8):1058–77.
[23] Nakashima M, Kato H. Development of real-time pseudo dynamic testing. Earthq Eng Struct Dynam 1992;21(1):79–92.
[24] Nakashima M, Masaoka N. Real-time on-line test for MDOF systems. Earthq Eng Struct Dynam 1999;28(4):393–420.
[25] Horiuchi T, Inoue M, Konno T, Namita Y. Real-time hybrid experimental system with actuator delay compensation and its application to a piping system with energy absorber. Earthq Eng Struct Dynam 1999;28(10):1121–41.
[26] Mercan O, Ricles JM. Experimental studies on real-time testing of structures with elastomeric dampers. J Struct Eng, ASCE 2009;135(9):1124–33.
[27] Christenson R, Lin Y, Emmons A, Bass B. Large-scale experimental verification of semiactive control through real-time hybrid simulation. J Struct Eng, ASCE 2008;134(4):522–34.
[28] Igarashi A, Iemura H, Suwa T. Development of substructured shaking table test method. In: Proceedings of the 12th World Conference on Earthquake Engineering.
[29] McCrum DP, Broderick BM. Evaluation of a substructured soft-real time hybrid test for performing seismic analysis of complex structural systems. Comput Struct 2013;129:111–9.
[30] Mosqueda G, Stojadinovic B, Mahin S. Implementation and accuracy of continuous hybrid simulation with geographically distributed substructures. Technical report. Berkeley, CA, USA: Earthquake Engineering Research Center, University of California; 2005.
[31] Schellenberg A, Mahin S, Fenves GL. Advanced implementation of hybrid simulation. Technical report. Berkeley, CA, USA: Pacific Earthquake Engineering Research Center, University of California; 2009.
[32] Zhang Z, Nielsen SRK, Blaabjerg F, Zhou D. Dynamics and control of lateral tower vibrations in offshore wind turbines by means of active generator torque. Energies 2014;7(11):7746–72.
[33] Pars LA. A treatise on analytical dynamics. Woodbridge: Ox Bow Press; 1979.
[34] IEC. 61400-1. Wind turbine part 1; design requirements. International Electrotechnical Committee; 2005.
[35] Batchelor GK. The theory of homogeneous turbulence. Cambridge: Cambridge University Press; 1953.
[36] Krenk S, Svendsen MN, Høgsberg J. Resonant vibration control of three-bladed wind turbine rotors. AIAA J 2012;50(1):148–61.
[37] Hansen MOL. Aerodynamics of wind turbines. London: Earthscan; 2008.
[38] Zhang Z, Nielsen SRK, Basu B, Li J. Nonlinear modeling of tuned liquid dampers (TLDs) in rotating wind turbine blades for damping edgewise vibrations. J Fluids Struct 2015;59:252–69.
[39] Sieros G, Chaviaropoulos P, Sørensen JD, Bulder BH, Jamieson P. Upscaling wind turbines: theoretical and practical aspects and their impact on the cost of energy. Wind Energy 2012;15(1):3–17.
[40] Jonkman J, Butterfield S, Musial W, Scott G. Definition of 5-MW reference wind turbine for offshore system development. Technical report, NREL/TP-500-38060. Golden, Colorado: National Renewable Energy Laboratory; 2009.
[41] Lackner MA, van Kuik G. A comparison of smart rotor control approaches using trailing edge flaps and individual pitch control. Wind Energy 2010;13(2–3):117–34.
[42] Ghosh A, Basu B. Alternative approach to optimal tuning parameter of liquid column damper for seismic applications. J Struct Eng ASCE 2007;133(12):1848–52.
[43] Ghosh A, Basu B. A closed-form optimal tuning criterion for TMD in damped structures. Struct Control Health Monitor 2007;14(4):681–92.
[44] Zhang Z, Li J, Nielsen SRK, Basu B. Mitigation of edgewise vibrations in wind turbine blades by means of roller dampers. J Sound Vib 2014;333(21):5283–98.